

(accepted, September, 2017)

Chapter

**FORMATION AND MAINTENANCE OF AN
AFRICAN EASTERLY WAVE MESOSCALE
CONVECTIVE SYSTEM IN 2004 OVER EAST
AFRICA AND THE ARABIAN PENINSULA**

Yuh-Lang Lin^{1,*}, James Spinks² and Bo-Wen Shen³

¹Department of Energy and Environmental Systems and
Department of Physics, North Carolina A&T State University
Greensboro, NC, US

²College of Technology, ECPI University, Greensboro, NC, US

³Department of Mathematics, San Diego State University,
San Diego, CA

ABSTRACT

The precursors of an intense coupled system (A04) of an African easterly wave (AEW) and a mesoscale convective system (MCS) over the lee of Darfur Mountains around 1800 UTC, August 12, 2004 were traced back to the southern Arabian Peninsula, Asir Mountains, and Ethiopian Highlands using gridded satellite (GridSat) data, European Centre

* Corresponding author: Email: ylin@ncat.edu.

Medium-Range Weather Forecast Intermediate (ERA-I) data, and the Advanced Research Weather Research and Forecasting (WRF) model simulated data. A vorticity budget analysis was performed to investigate the dynamics and mechanisms that contributed to the enhancement of A04's vorticity perturbation. It was found that convergence of southeasterly and northwesterly wind from anticyclones over Arabian and Indian Ocean generates cyclonic vorticity over the southern Arabian Peninsula that was advected by an easterly wind maximum embedded within the African easterly jet. Convergence and vorticity advection were the most important factors to the formation of A04's vorticity perturbation, while cloud clusters were generated by diurnal heating over the Asir Mountains, Ethiopian Highlands and Darfur Mountains. Both vorticity perturbation and cloud clusters went through their formation and propagation phases, intensified by lee vortices, and then eventually merged into an AEW-MCS system on the lee of the Darfur Mountains, consistent with the conceptual model proposed in Lin et al. (2013).

1. INTRODUCTION

Earlier studies showed that African easterly waves form between May and October when large-scale environmental conditions favor the existence of the African jet. African easterly waves may propagate westward across the tropical and subtropical North Atlantic and reach the Caribbean Sea and western North Atlantic. Some African easterly waves become hurricanes. In particular, observational analyses indicated that AEWs possess the following basic characteristics (Reed et al., 1977; Burpee, 1974; see review in Chen, 2006): (1) a propagation speed of $7 - 9 \text{ ms}^{-1}$, (2) a wavelength of $\sim 2000 - 4000 \text{ km}$, and (3) propagating along the rainy zone and to the south of the African easterly jet (AEJ) around 10°N (AEW_s) or along the Saharan thermal low near 20°N (AEW_n).

Several mechanisms have been proposed for the formation of AEWs in previous studies: (1) release of barotropic-baroclinic instability (Charney-Stern 1962, Burpee 1972, Chen 2006), which is more applicable to the AEW_s; (2) release of baroclinic instability (Chang 1993; Thorncroft 1995) which is more applicable to the AEW_n. Also included is the release of the proclaimed African Easterly Jet (AEJ) instability (e.g., Simmons 1977; Thorncroft and Hoskins 1994a, b; Grist et al., 2002), which is assisted by

the baroclinicity associated with the Sahara Desert; (3) latent heating (e.g., Hsieh & Cook 2005, 2007; Thorncroft et al. 2008); and (4) orographic forcing (Mozer & Zehnder 1996; Lin et al., 2005, 2013; Mekonnen et al. 2006; Laing et al. 2012). In later work of pre-Debby (2006) AEW-MCS (Lin et al., 2013), a conceptual model (Figure 1) was proposed to illustrate the role of the interaction between northeasterly Shamal wind and southwesterly wind from the India Ocean anticyclone in producing cyclonic vorticity perturbation, which served as the precursor of the AEW, over the southern Arabian Peninsula. More details on the conceptual model are provided below.

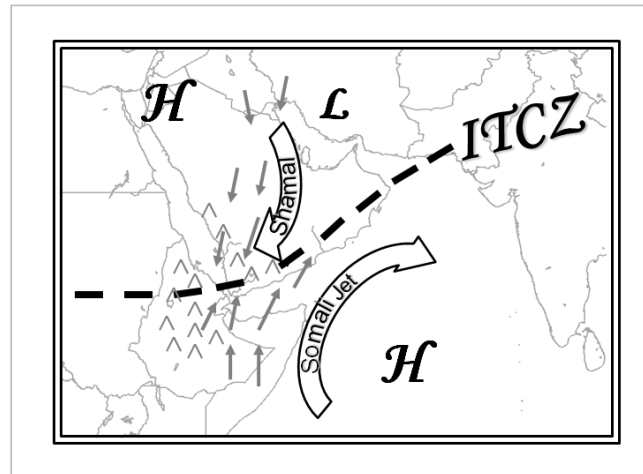


Figure 1. A conceptual model of the generation of cyclonic vorticity perturbations and convective cloud clusters preceding the pre-Debby (2006) AEW-MCS system, as proposed in Lin et al. (2013). The sources of the convective cloud clusters and vorticity perturbations were attributed to the cyclonic convergence of northeasterly Shamal wind and the Somali jet, especially when the Mediterranean High shifted toward east with high pressure ridge extended farther to the southeast and the Indian Ocean high strengthened and its associated Somali jet penetrated farther to the north. The cyclonic vorticity perturbations were strengthened by the vorticity stretching associated with convective cloud clusters and the convective cloud clusters are strengthened by the diurnal convection over the Sarawat Mountains, Asir Mountains, Ethiopian Highlands, and Darfur Mountains downstream of the genesis region (i.e., southwest Arabian Peninsula).

AEWs are often associated with mesoscale convective systems (MCS) while they travel westward (e.g., Payne & McGarry, 1977; Laing & Fritsch, 1993; Fink & Reiner, 2003). This helps alter convection and rainfall over the African continent daily (e.g., Carlson, 1969) and makes AEWs detectable from satellite imagery. MCSs tend to occur in preferred regions of AEWs: at or ahead of the AEW trough in the vicinity of the intertropical convergence zone (ITCZ), and collocated with the trough over the ocean. Hill and Lin (2003) and Lin et al. 2005, back-tracked the pre-Alberto AEW-MCS (2000) precursor to the Ethiopian Highlands, while Mekonnen et al. (2006) found that the Darfur Mountains are particularly important for providing convective precursors that propagate westward and trigger AEWs downstream. Although the MCS has been used as proxy for detecting the AEWs, there are distinct features of the convective system and the wave perturbation (e.g., Lin et al. 2013). Thus, it is important to trace both of them or their individual precursors near their source regions.

Based on statistical analysis of AEW activities, Hodges and Thorncroft (1997) showed that northern Africa could be divided into areas of genesis or lysis regions for growing or dissipating convection, respectively. The areas are determined by using the coldest cloud-top temperatures to track several MCSs across northern Africa where the appropriate convective activities were identified. Other studies have also shown that most MCSs formed in baroclinic zones and downstream of mountain ranges (Laing & Fritsch, 1993; Laing et al., 2012), such as the case over northern Africa during the Northern Hemisphere summer months.

The pre-tropical storm Debby (2006) AEW (also denoted as pre-Debby AEW hereafter) was traced back to a vorticity genesis region in eastern North Africa by Lin et al. (2013). This region is located over the southern Arabian Peninsula and was investigated to see formation and evolution of the pre-Debby AEW-MCS. In this study, we will concentrate on the origin of a coupled *AEW-MCS in August of 2004* (denoted as A04, hereafter) while taking a similar approach that was used to explain vorticity generation in Lin et al. (2013). A04's MCS/convective clusters and A04's AEW/vorticity perturbation will be examined to understand the mechanisms that generate these systems. The reason for investigating this

A04 AEW-MCS is that its characteristics are very similar to those of pre-Debby AEW-MCS, but did not trigger tropical cyclone over the Atlantic.

Eastern North Africa and the Arabian Peninsula include mountains that will have an effect of the generated vorticity and MCSs, especially during diurnal cycles. The influence of orography has been observed in the development of lee vortices and, subsequently to AEWs (Hill and Lin 2003). This study will focus on the analysis of wind and vorticity fields along with diabatic processes to identify A04's origins to verify the conceptual model proposed in Lin et al. (2013; Figure 1) for the generation of AEW precursor (cyclonic vorticity perturbation) and convective cloud clusters preceding the pre-Debby (2006) AEW-MCS system. In Lin et al.'s conceptual model, the sources of the convective cloud clusters and vorticity perturbations are attributed to the cyclonic convergence of northeasterly Shamal wind and the Somali jet, especially when the Mediterranean High shifts toward east with high pressure ridge extended farther to the southeast and the Indian Ocean high strengthened and its associated Somali jet penetrated farther to the north. The cyclonic vorticity perturbations are strengthened by the vorticity stretching associated with convective cloud clusters and the convective cloud clusters are strengthened by the diurnal convection over the Sarawat Mountains, Asir Mountains, Ethiopian Highlands, and Darfur Mountains downstream of the genesis region, i.e., the southwest Arabian Peninsula.

The rest of this paper is organized as follows: section 2 describes data used and the experiment design for the numerical case study. Section 3 presents the results with two subsections, including observational analysis from satellite and reanalysis data in section 3.1 and numerical results from the model in section 3.2. Concluding remarks are provided at the end of the paper.

2. DATA AND EXPERIMEN DESIGN

In order to investigate the origins and propagation of the AEW and MCS, various datasets were used to identify case study A04. For AEW

convection analysis, observational globally gridded satellite (GridSat) data from the National Climatic Data Center (NCDC) at an 8-km spatial resolution and 180-min temporal resolution (Knapp et al., 2011) were used. The GridSat data that serve as reliable observations for cloud clusters are analyzed along with the global European Centre Medium-Range Weather Forecast Intermediate (ERA-I) dataset at a resolution of $0.75^\circ \times 0.75^\circ$ and a time interval of 6 h (Dee et al. 2011). Using the ERA-I, analysis was performed to track AEWs and MCSs and investigate the regions of genesis. Daily precipitation associated with A04 is illustrated using the data from the National Oceanic and Atmospheric Administration Climate Prediction Center's Famine Early Warning System (NOAA CPC FEWS). Since MCSs are associated with precipitation, the NOAA CPC FEWS data may provide information on MCSs and can be inter-compared with the GridSat and ERA-I to track A04's MCS.

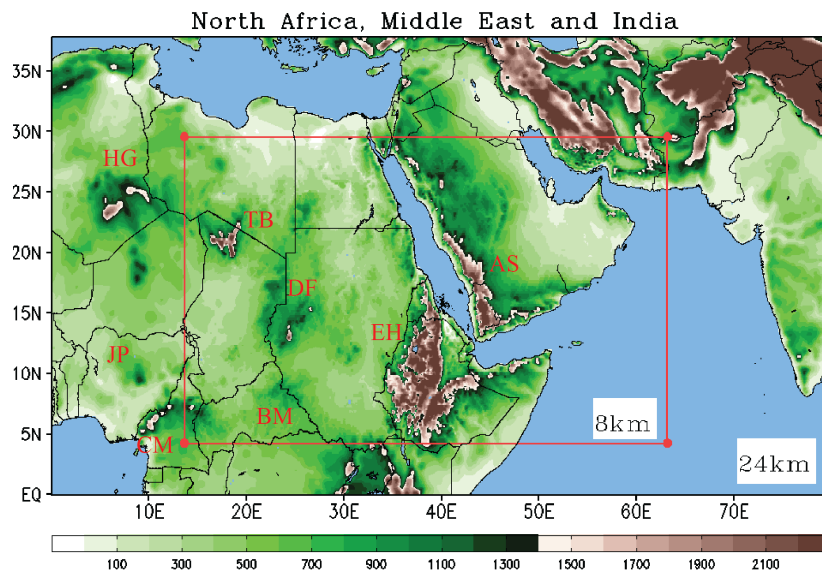


Figure 2. WRF simulated geography for Africa (north of 0°) and southern Arabia Peninsula. Labels indicate major geographic features: *AS* Asir Mountains, *BM* Bongo Massif, *CM* Cameron Highlands, *DF* Darfur Mountains, *EH* Ethiopian Highlands, *HG* Hoggar Mountains, *JP* Jos Plateau, and *TB* Tibesti Mountains. The outer domain of the simulation is 24 km and the inner domain (red lines) is 8 km resolution.

Once a case study is verified from observational analysis, the Advanced Research Weather Research and Forecasting (WRF) model version 3.3.1 (Skamarock et al. 2008) will be used to simulate the phenomena. The WRF model is a numerical weather prediction (NWP) and atmospheric simulation system designed for both research and operational applications. The WRF model is a compressible, three-dimensional, nonhydrostatic model using terrain-following coordinates. The governing equations for WRF are written in flux-form with conserved mass and dry entropy. In the numerical model, the third-order Runge-Kutta time scheme was employed and fifth and third order advection schemes were chosen for the horizontal and vertical directions, respectively. An open (radiative) lateral boundary condition was used in the north-south direction, a free-slip condition was used for the lower boundary condition, and a periodic boundary condition was used in the east-west direction.

Figure 2 illustrates the domains used in WRF to simulate A04. The 24-km outer domain consist of 350 x 180 grid points, 38 vertical levels, and 120 second time steps. The 8-km inner nested domain consist of 652 x 352 grid points, 38 vertical levels, and 40 second time steps. The physics options for both domains include: Goddard microphysics, RRTM longwave radiation, Duhdia shortwave radiation, Mellor-Yamada-Janjic PBL physics, and Betts-Miller-Janjic cumulus parameterization.

3. RESULTS

3.1. Analysis from Observations and ERA-I

3.1.1. Tracking the Convection of A04

A04 was identified by analyzing Hovmoller diagrams from Gridsat brightness temperature and comparing it with ERA-I cloud cover and relative vorticity. The idea of this comparison was to note regions of intense easterly waves that originated from the Arabian Peninsula (50°E) and propagated into East Africa. Figure 3 illustrates A04's MCS that was formed at 0600 UTC, August 9, 2004 (for simplicity, it is denoted as

09/06Z hereafter). The Gridsat and ERA-I's cloud cover compares well, thus giving confidence in the simulated MCS from the ERA-I is realistic enough to proceed with the case study of A04.

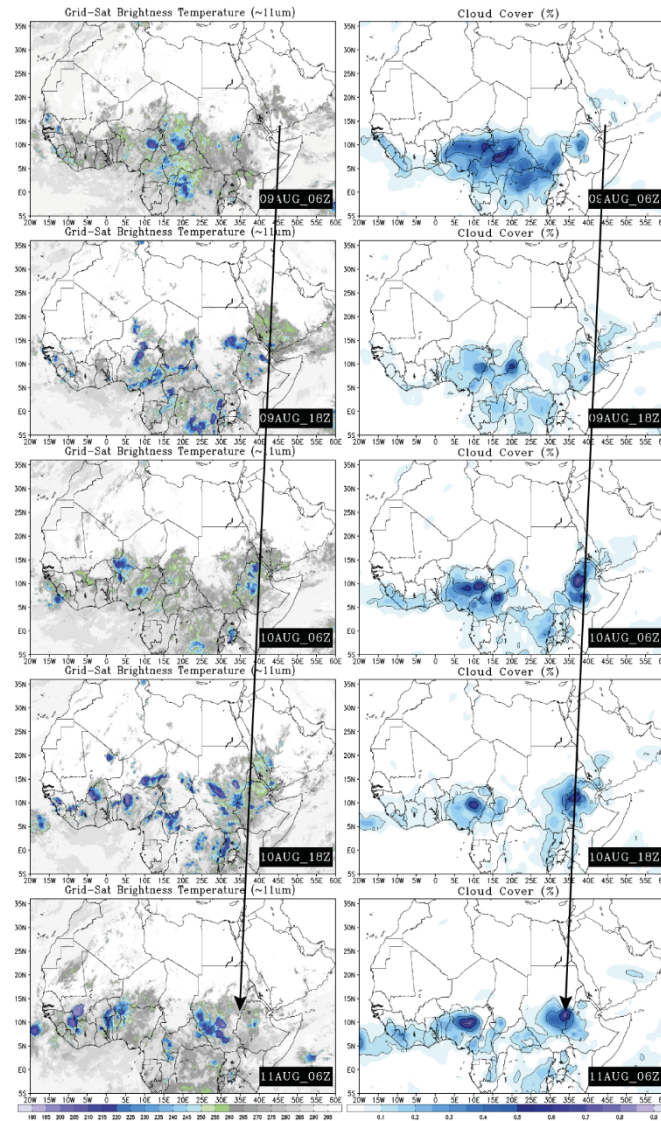


Figure 3. (a) Gridsat (left column) brightness temperature versus ERA-I (right column) total cloud cover (%). Black line denotes track of case study A04 between 08/09/06Z to 08/11/06Z every 12h.

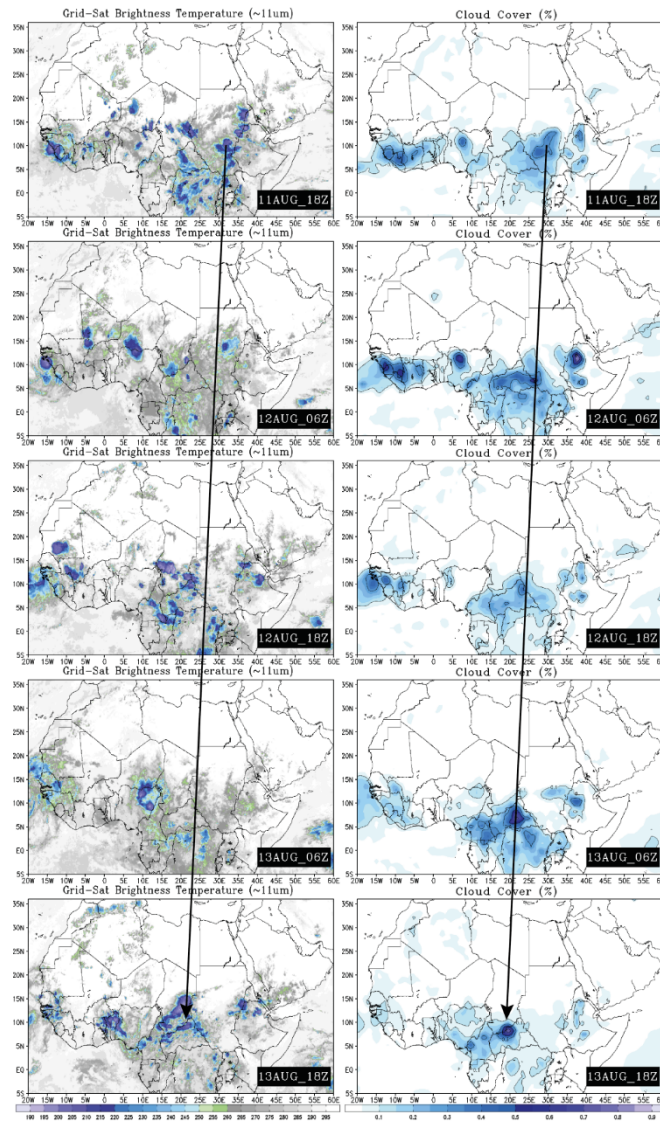


Figure 3. (b) Gridsat (left column) brightness temperature versus ERA-I (right column) total cloud cover (%). Black line denotes track of case study A04 between 08/11/18Z to 08/13/18Z every 12h.

In Figure 3a, the associated MCS for A04 can be seen in both from Gridsat and ERA-I at 9/06Z over the southern Arabian Peninsula. The MCS propagates over the Asir Mountains at 9/18Z and the Ethiopian Highlands at 10/06Z where orographic effects will enhance the convection. At 10/06Z, there is a noticeable convective cloud burst over the Ethiopian Highlands. The MCS begins to weaken in the Gridsat at 11/06Z, but remains intense in the ERA-I. In Figure 3b at 11/18Z, the MCS propagates away from the Ethiopian Highlands crossing Sudan at 12/06Z and 12/18Z. In the Gridsat at 13/06Z the MCS has entered a dissipation phase, before there is another convective cloud burst of the Darfur Mountains and 13/18Z. The ERA-I does not show dissipation of convection at 13/06Z, but did resolve the convective cloud burst at 13/18Z.

Overall, the ERA-I compared well with convection from Gridsat, which showed the propagation of A04's associated MCS. Maintenance of convection based on satellite can be attributed to orographic effects from the Asir Mountains, Ethiopian Highlands, and Darfur Mountains, especially during diurnal cycles.

To further strengthen the confidence of A04 from the ERA-I being realistic, the NOAA CPC FEWS daily precipitation is plotted with ERA-I 600 mb geopotential heights (Figure 4). On the 8th and 9th of August over the southern Arabian Peninsula, an inverted trough can be seen with little accumulated precipitation associated with it. On the 10th, the trough is over the Ethiopian Highlands where precipitation accumulation is increasing. There is a large daily accumulated precipitation flux on the 11th as the trough begins to strengthen. The trough continues to mature on the 12th, but the accumulated precipitation decreased. This is consistent with the Gridsat showing weak convection crossing Sudan at 12/06Z and 12/18Z in Figure 3b. By the 13th, close contours of geopotential heights at 600 mb located at (7°N, 19°E) indicate a mature easterly wave organizing on the lee side of the Darfur Mountains. It is noteworthy to see during the daily averages of geopotential that a subtropical high (Arabian High) over the Arabian Peninsula is present. The pressure increases per day for the Arabian in which it will also increase easterly flow on the southern rim of the subtropical anticyclonic zone over southern Arabia and Easter Africa.

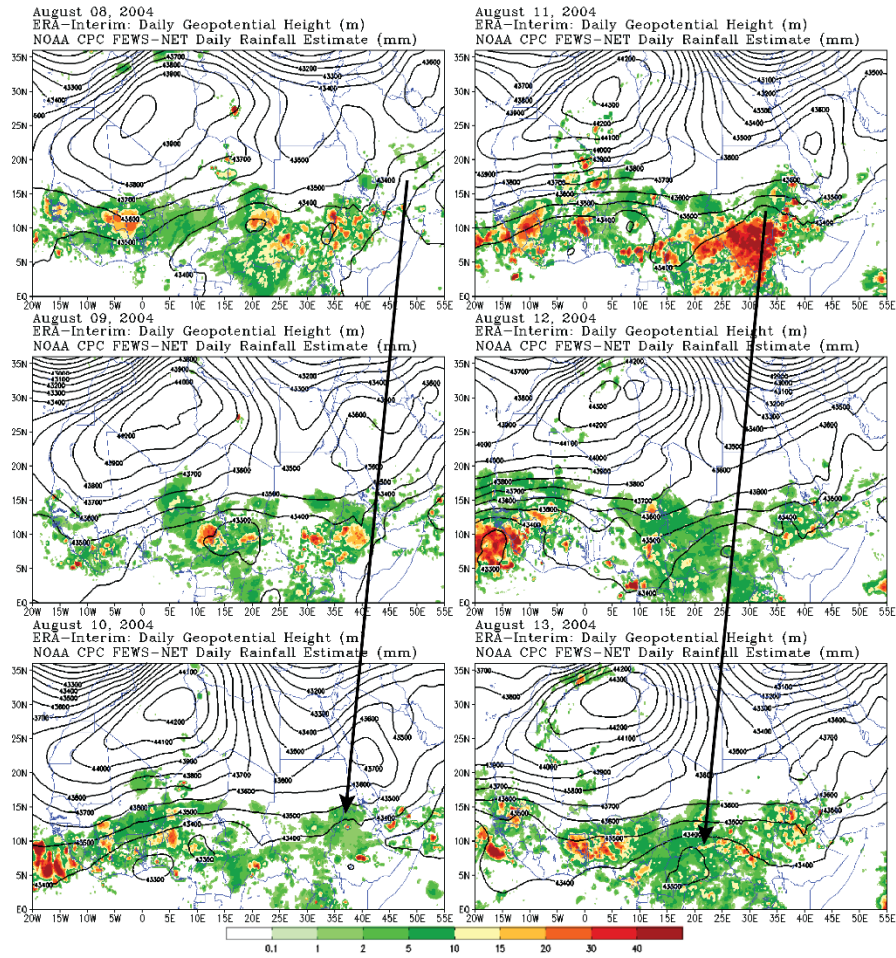


Figure 4. NOAA CPC FEWS daily precipitation (mm) shaded and ERA-I 600 mb daily geopotential heights (m) in black contours between August 8th and August 13th. Black line denotes the location of A04.

3.1.2. Relative Vorticity Analysis Using ERA-I

In section 3.1.1, A04's convective cloud clusters were traced Gridsat and ERA-I total cloud cover. Difficulty with tracking clouds clusters is due to formation and dissipation of clouds with the diurnal cycle. When

convection is weak, cloud tops are not as cold according to brightness temperature. This suggests a weak phase for the MCS, but the associated vorticity may still be present for easier tracking. Figure 5 is the 600 mb relative vorticity field for the ERA-I. The band of positive relative vorticity between 5°N and 15°N is the preferred region of easterly wave propagation. Starting on 9/06Z at (14°N, 47°E), there is strong positive vorticity over the southern Arabian Mountains, but the convection is weak according to the GridSat and ERA-I cloud cover analysis at the same time. This vorticity propagates into the East Africa at 10/06Z where it is enhanced by the orographic effects from the Asir Mountains and Ethiopian Highlands. As the vorticity perturbation continue to propagate away from the Ethiopian Highlands at 10/18Z, it begins to strengthen and mature. At 11/18Z, the system is becoming more organized with the convection produced from the Ethiopian Highlands and continues its propagation across Sudan to the Darfur Mountains by 12/18Z. Once the system reaches the Darfur Mountains, it organizes again from orographic effects and matures into an AEW at 13/06Z. At 13/18Z, A04's MCS (Figure 2b) and A04's AEW are now a coupled system and is part of a Rossby wave that extends from West Africa at (15°N, 13°W) to the southern Arabian Peninsula at (12°N, 47°E). From Arabia (47°E) to the lee side of the Darfur Mountains (20°E) is about 2970 km and it took A04's vorticity perturbation 108 h to travel. A04 has a propagation speed of 7.6 m s⁻¹, which is slightly faster than the wave propagation speed observed by (Burpee 1974; Reed et al. 1977; and Chen 2006).

The vorticity budget will be used to explain the generation of A04's vorticity perturbation over the Arabian Peninsula. Using the vorticity equation from (Bluestein 1992) we have:

$$\frac{\partial \zeta}{\partial t} = -\mathbf{V} \cdot \nabla \zeta - \omega \frac{\partial \zeta}{\partial p} - v\beta - (\zeta + f)\nabla \cdot \mathbf{V} - \hat{k} \cdot \nabla \omega \times \frac{\partial \mathbf{V}}{\partial p} + \hat{k} \cdot \nabla \times Fr \quad (1)$$

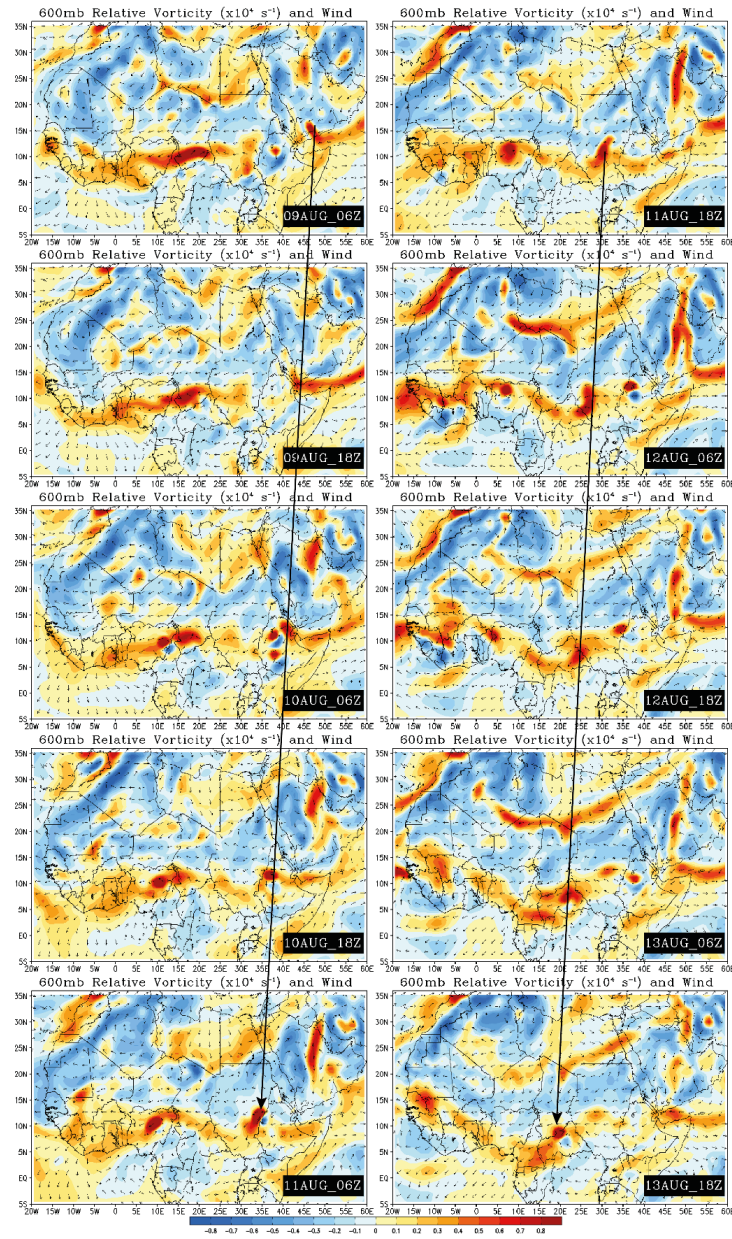


Figure 5. ERA-I 600 mb relative vorticity (s^{-1}) and wind vectors between 08/09/06Z to 08/13/18Z every 12 h. Red (blue) shade is for positive (negative) vorticity. Black line represents the track of A04.

Equation (1) examines vorticity generation from a mechanical perspective. After analysis of the relative vorticity field, earliest detection of A04's vorticity perturbation was at 09/00Z. Magnitudes for local rate of change, horizontal vorticity advection, vertical advection, and divergence are at an order of 10^{-10} s^{-2} . The local rate of change in vorticity, shows the evolution of vorticity between 08/18Z to 09/06Z (Figure 6a). Central differencing in time from the local rate of change yields the detection time of A04's vorticity perturbation located (15°N , 47°E). The positive horizontal vorticity advection has the highest magnitude between all the terms (Figure 6b). Easterly zonal wind flow will aid advection of relative vorticity, therefore adding to the intensity of the magnitude of horizontal advection. The positive vorticity advection of A04 is located at (15°N , 48°E) at 09/00Z. The presence of the Asir Mountains induces vertical motion of vorticity that is generated from the diurnal cycle (Figure 6c). The source of vertical motion is also associated with convection generated from ITCZ heating.

Preexisting relative vorticity (ζ) is in each term of Eq. (1), but the divergence term $-(\zeta + f)\nabla \cdot \mathbf{V}$ can be split into two separate terms with ζ and f , respectively. Since f is dependent on the Earth's rotation, then convergence and f will generate vorticity. Figure 6d at 09/00Z, shows A04's vorticity perturbation being generated over the Arabian Peninsula located at (15°N , 48°E). Comparisons were done (not shown) between the magnitudes of $f\nabla \cdot \mathbf{V}$ and $\zeta\nabla \cdot \mathbf{V}$ and it was concluded that $f\nabla \cdot \mathbf{V}$ had the higher magnitude. Given this result, $\zeta\nabla \cdot \mathbf{V}$ became negligible in contribution to vorticity generation for A04. The sources of the vorticity perturbations were attributed to convergence of southeasterly Shamal winds, which is associated with the Arabian high and the northwesterly Somali jet winds, that is associated with the Indian Ocean high (Lin et al. 2013). These interaction increases vorticity generation until the vorticity is advected by the mean easterly wind flow of the AEJ.

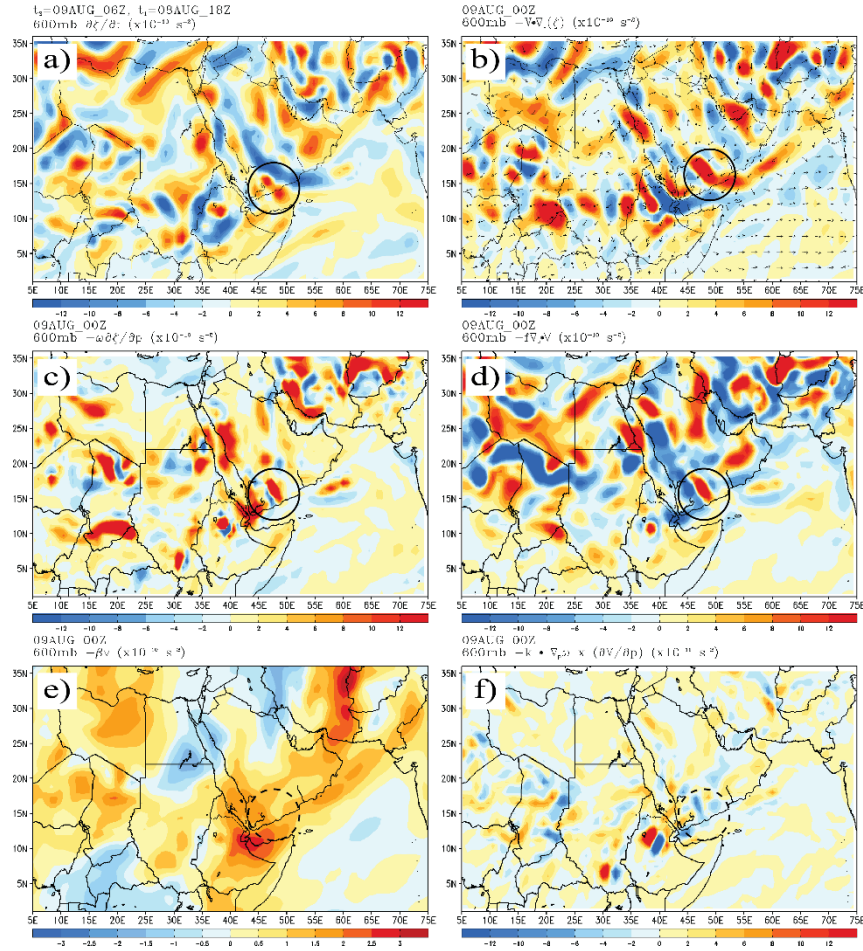


Figure 6. ERA-I 600 mb vorticity budget analysis of (a) local rate of change ($\times 10^{-10} \text{ s}^{-2}$) for $t_2 = 09/06Z$ and $t_1 = 08/18Z$, (b) vorticity advection ($\times 10^{-10} \text{ s}^{-2}$) at 09/00Z, (c) vertical vorticity advection ($\times 10^{-10} \text{ s}^{-2}$) at 09/00Z, (d) divergence ($\times 10^{-10} \text{ s}^{-2}$), (e) beta effect ($\times 10^{-10} \text{ s}^{-2}$), and (f) tilting ($\times 10^{-11} \text{ s}^{-2}$). The black circles denote where A04 is located.

Table 1. Physics parameterization schemes used to test the performance of the WRF model

Experiment	Microphysics	Cumulus
A.	Thomson	Kain-Fritsch
B.	Thomson	Grell 3d ensemble
C.	WSM-6 Class	Kain-Fritsch
D.	WSM-6 Class	Grell 3d ensemble
E.	Goddard	Kain-Fritsch
F.	Lin	Grell 3d ensemble
G.	Goddard*	Betts-Miller-Janjic*
H.	Lin	Betts-Miller-Janjic

* Combination G is used for the main simulation.

The beta effect (Figure 6e) shows the drifting planetary vorticity advection. The meridional gradient of planetary vorticity is high over the Arabian Peninsula in comparison to East Africa because of the southerly meridional winds over the Arabian Peninsula are strong. The southerly winds are associated with the Arabian high and Shamal winds. Even though the magnitudes of the beta term are on the same order of $-\mathbf{V} \cdot \nabla \zeta$, $-\omega \frac{\partial \zeta}{\partial p}$, and $-f \nabla \cdot \mathbf{V}$; the values are smaller than the respective terms. The tilting term (Figure 6f) is at an order of 10^{-11} s^{-2} . and therefore, is negligible in comparison with the higher ordered terms.

The relative vorticity field and budget analysis of A04's vorticity perturbation using the ERA-I provided realistic details about wave genesis over the Arabian Peninsula. It was found that A04's vorticity perturbation was generated around 09/00Z and was a mature AEW at 13/18Z. This will be essential for setting up a time interval to simulate A04 using the WRF model.

3.2. WRF Simulated Results

3.2.1. Model Performance and Comparison to ERA-I

The WRF simulation uses ERA-I at 08/00Z to initialize and is ran until 15/00Z, outputted every 3 h. A series of experiments were performed to

identify possible physics combinations that would best represent A04. Figure 7 illustrates the various combinations using daily rain totals and 600 mb geopotential height with the corresponding combinations in Table 1. Comparing Figure 7 to Figure 4, it can be seen how the model performed against the NOAA CPC FEWS daily precipitation and ERA-I geopotential height. Using precipitation as a diagnostic variable will eliminate physics combinations that may have simulated A04 too aggressively or not aggressive enough.

The most aggressive combinations for precipitation came from WSM 6 Class, Thompson, Kain-Fritsch, and Grell 3d ensemble (Figure 7a-d). The precipitation is a result from convection being over intensified or producing unrealistic convective processes. These results do not compare well with Figure 4. The Goddard and Lin schemes (Figures 7e-h) performed better in terms of precipitation reliability and cumulus schemes were narrowed down to Betts-Miller-Janic (Figure 7g and h). After close inspection and comparison between physics combinations, the Goddard and Betts-Miller-Janic scheme were used as the control simulation for this case study.

The calculated relative vorticity magnitudes are stronger in the WRF simulation in comparison to the ERA-I. This is due to increased grid resolution of 8 km. In Figure 8, the WRF simulated 600 mb horizontal wind (Figure 8a and b) can be compared with the ERA-I data (Figure 8c and d) to show the intensity difference between models. The components of relative vorticity are $\partial u/\partial y$ and $\partial v/\partial x$. An increase of intensity from either component will intensify the overall relative vorticity. The most noticeable difference of intensity comes from the simulated zonal wind (Figure 8a) versus the ERA-I zonal wind (Figure 8c). The easterly wind between 9°N and 21°N illustrates the AEJ. Spinks et al. (2014) investigated the AEJ over East Africa and found a local wind maximum embedded within the AEJ centered at (14°N, 35°E). This local wind maximum in East Africa (LMW_E), is present in the simulation and ERA-I, but the intensity is significantly different. For the WRF simulation and

ERA-I, the intensity of the LMW_E is 12 to 14 m s⁻¹ and 10 to 12 m s⁻¹, respectively. Westerly wind has a stronger presence over East Africa centered at (6°N, 20°E) in the simulation versus the ERA-I. The magnitude of the easterly wind is stronger over the Arabian Peninsula as well.

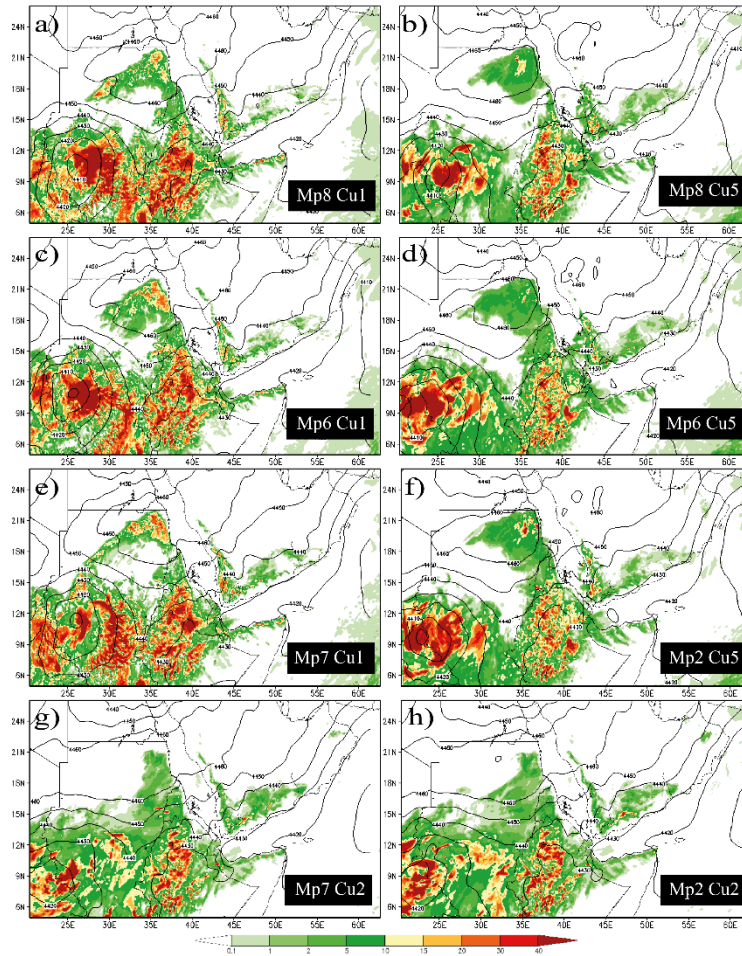


Figure 7. WRF simulated daily precipitation (mm) of August 12, 2004 (shaded) and 600 mb geopotential height (m) in black contours for multiple physics schemes. The corresponding combination of physic schemes can be seen in Table 1.

The reason for the zonal wind magnitude increase from the simulation versus the ERA-I, is due to the geopotential height being stronger. The Arabian high can be seen in the WRF simulation centered at (21°N, 37°E) (Figure 8a) and the ERA-I centered at (21°N, 43°E) (Figure 8c). The geopotential height vales are stronger in the WRF simulation for the Arabian high by about 1000 m and the structure of the anticyclone is broader. The increased geopotential values will, induce a stronger positive meridional geopotential gradient, which will increase the easterly zonal magnitudes that influences relative vorticity intensity over East Africa and the Arabian Peninsula.

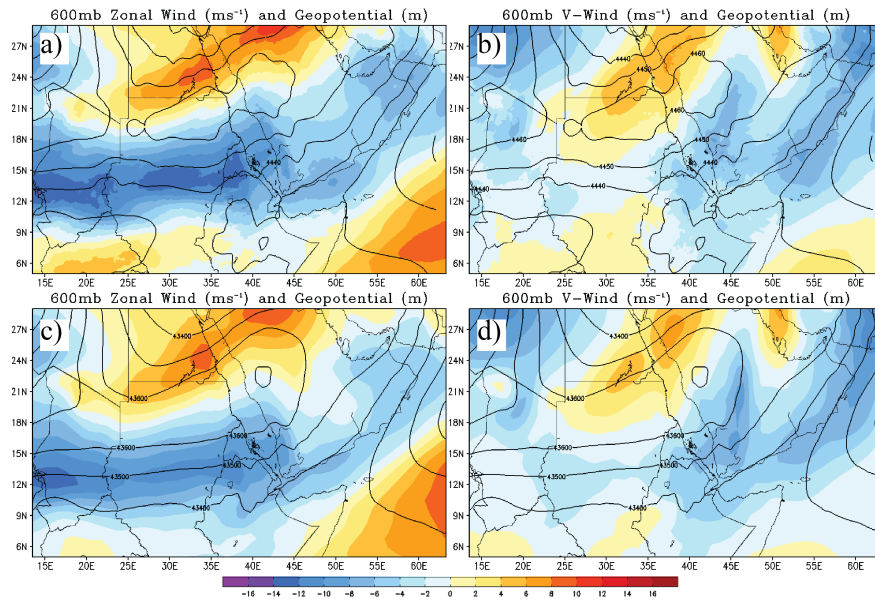


Figure 8. Six-day average between 09/00Z and 15/00Z of WRF simulated 600 mb (a) zonal wind (m s^{-1}) and (b) meridional wind (m s^{-1}) shaded with geopotential height (m) in black contours. ERA-I is averaged for the same time for 600 mb (c) zonal wind (m s^{-1}) and (d) meridional wind (m s^{-1}) shaded with geopotential height (m) in black contours.

The meridional wind comparison between the WRF simulation and ERA-I (Figures 8b and 8d), reveals little difference of magnitudes. This means that the relative vorticity magnitude increase will come from the zonal wind component. The northerly wind over the Arabian Peninsula center at (20°N, 43°E) is associated with the Arabian high. The northerly jet located in southeast Arabian is from the gradient of the subtropical high system and Indian Monsoon low converging.

The relative vorticity magnitudes will be higher in the WRF simulation versus the ERA-I. The WRF simulation will also resolve more vorticity process, providing information that cannot be completely from the ERA-I. The next section will illustrate the WRF simulated vorticity and the 3 stages of case study A04.

3.2.2. Three Stages of A04: Formation, Merger, Mature

Vorticity budget analysis at 600 mb from the WRF simulation will reveal genesis mechanisms that will explain the origin of A04's vorticity perturbation. In section 3.1.2, budget analysis was performed using the ERA-I. In section 3.2.1, it was explained that the calculated relative vorticity in the WRF simulation will have a higher magnitude than the vorticity from the ERA-I. In Figure 9, the vorticity budget from the simulation uses the same variables as Eq. (1) in Figure 6 from the ERA-I. The origin of A04's vorticity perturbation was traced to 9/00Z, so we used central differencing of time for the local rate of change, where $t_1 = 08/21Z$ and $t_2 = 09/03Z$. The magnitudes of vorticity show an increase of intensity in comparison to the local rate of change in the ERA-I. A04 is located at (15°N, 47°E) and the order of the local rate of change is as high at 10^{-9} s^{-2} . The vorticity advection has the highest order and magnitude between all terms, with Figure 9b being plotted at 10^{-9} s^{-2} . The high magnitudes of vorticity advection can be explained by preexisting vorticity perturbations along the ITCZ. Positive vorticity advection is dominative along the southern Arabian Mountains and will be enhance from orographic effects and mean easterly wind flow in the mid-troposphere. The increased meridional zonal gradients from the relative vorticity calculation is the major component of the enhance magnitude for vorticity advection. It was

shown in Figure 8, that the meridional wind component has little increase of magnitude to vorticity, so the meridional vorticity advection component of $-\mathbf{V} \cdot \nabla \zeta$ is smaller than the zonal component. Instead, the meridional component is important for cyclonic vorticity generation from to the interactions of the northerly and southerly winds converging at (15°N, 47°E).

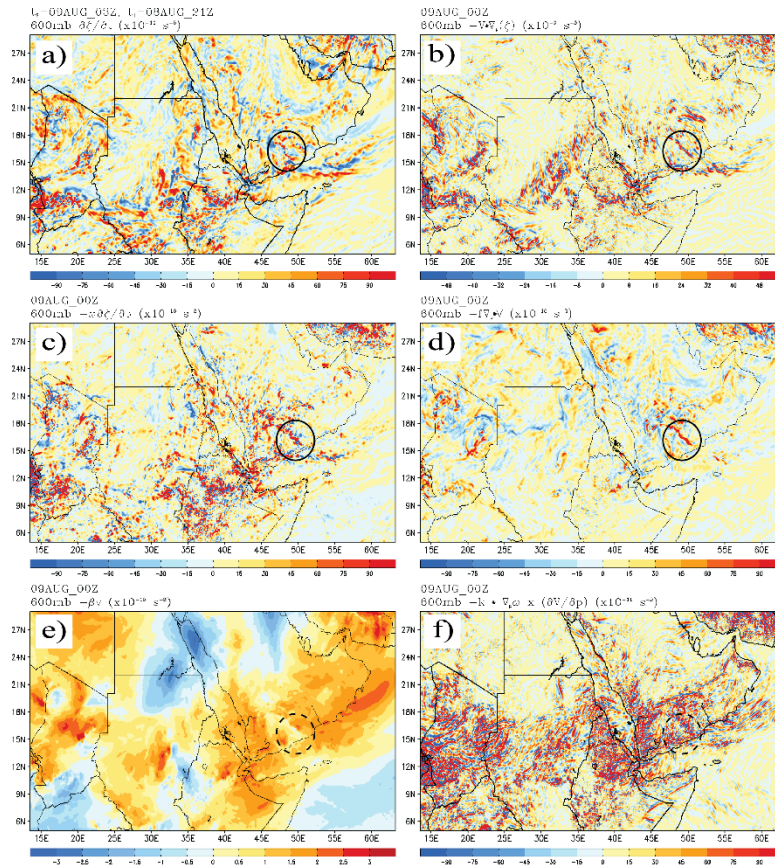


Figure 9. WRF simulated 600 mb vorticity budget analysis of (a) local rate of change ($\times 10^{-10} s^{-1}$) for $t_2 = 09/06Z$ and $t_1 = 08/18Z$, (b) vorticity advection ($\times 10^{-10} s^{-1}$) at 09/00Z, (c) vertical vorticity advection ($\times 10^{-10} s^{-1}$) at 09/00Z, (d) divergence ($\times 10^{-10} s^{-1}$), (e) beta effect ($\times 10^{-10} s^{-1}$), and (f) tilting ($\times 10^{-11} s^{-1}$). The black circles denote where A04 is located.

The vertical vorticity advection illustrates where the highest magnitude of vorticity will be advected into the atmosphere. For A04, the southern Arabian Mountains was the source of vertical motion induced by the diurnal cycle and easterly wind flow over the mountains. The term $-\omega \frac{\partial \zeta}{\partial p}$ does not explain generation of vorticity, but it does explain the enhancement by vertical advection.

The divergent term $-(\zeta + f)\nabla \cdot \mathbf{V}$ will be the most important factor to illustrate vorticity generation. Using ζ infers preexisting vorticity and ζ is less than f on a synoptic scale, so it can be negligible for the generation of A04's vorticity perturbation. Thus, we are left with $-f\nabla \cdot \mathbf{V}$, which explains the generation of relative vorticity due to convergence. In Figure 9d, A04 is located at (15°N, 48°E) with strong magnitudes of convergence over the southern Arabian Mountains.

The beta term (Figure 9e) and tilting term (Figure 9f) has the smallest magnitudes and therefore are not significant for the generation of vorticity. The terms $\frac{\partial \zeta}{\partial t}$, $-\mathbf{V} \cdot \nabla \zeta$, and $-f\nabla \cdot \mathbf{V}$ are the most significant in magnitude and clearly shows how A04 vorticity is generated from convergence, the advection of vorticity, and the local rate of change of vorticity. The diurnal cycle will help induce orographic generated vorticity along with convergence of the Shamal northerlies and southerlies from the Indian Ocean high. The vorticity advection has the highest order and works complementary with the easterly flow over southern Arabia.

Lin et al. (2005) found that there are two modes of the pre-Alberto (2000) MCSs embedded within the AEW structure: a stationary mode and a propagating mode. The stationary mode exists over the Ethiopian Highland on a diurnal variation due to sensible heating over the high terrain. The propagation mode coincides with the propagation and generation of AEWs in the vicinity of the Ethiopian Highlands. In a later study, Lin et al. (2013) found a stationary mode of over the southern Arabian Mountains, which was the genesis region for the pre-Debby AEW-MCS precursor. The two stationary modes of vorticity generation over the Ethiopian Highlands and Arabian Mountains influence the genesis of A04's vorticity perturbation.

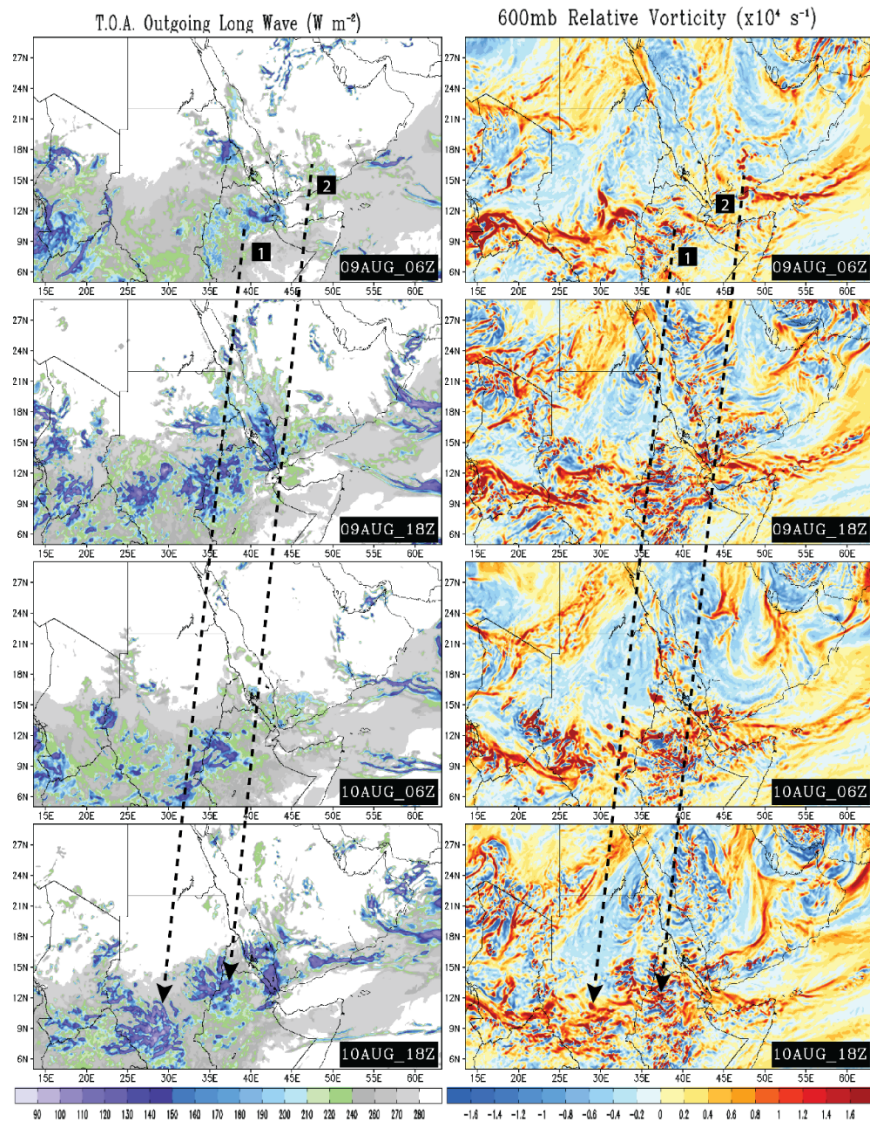


Figure 10. (a) WRF simulated top of the atmosphere outgoing long wave radiation ($W s^{-2}$) shaded in the left column and 600 mb relative vorticity ($10^{-4} s^{-1}$) shaded in the right column. Time interval is between /08/09/06Z to 08/10/18Z every 12 h.

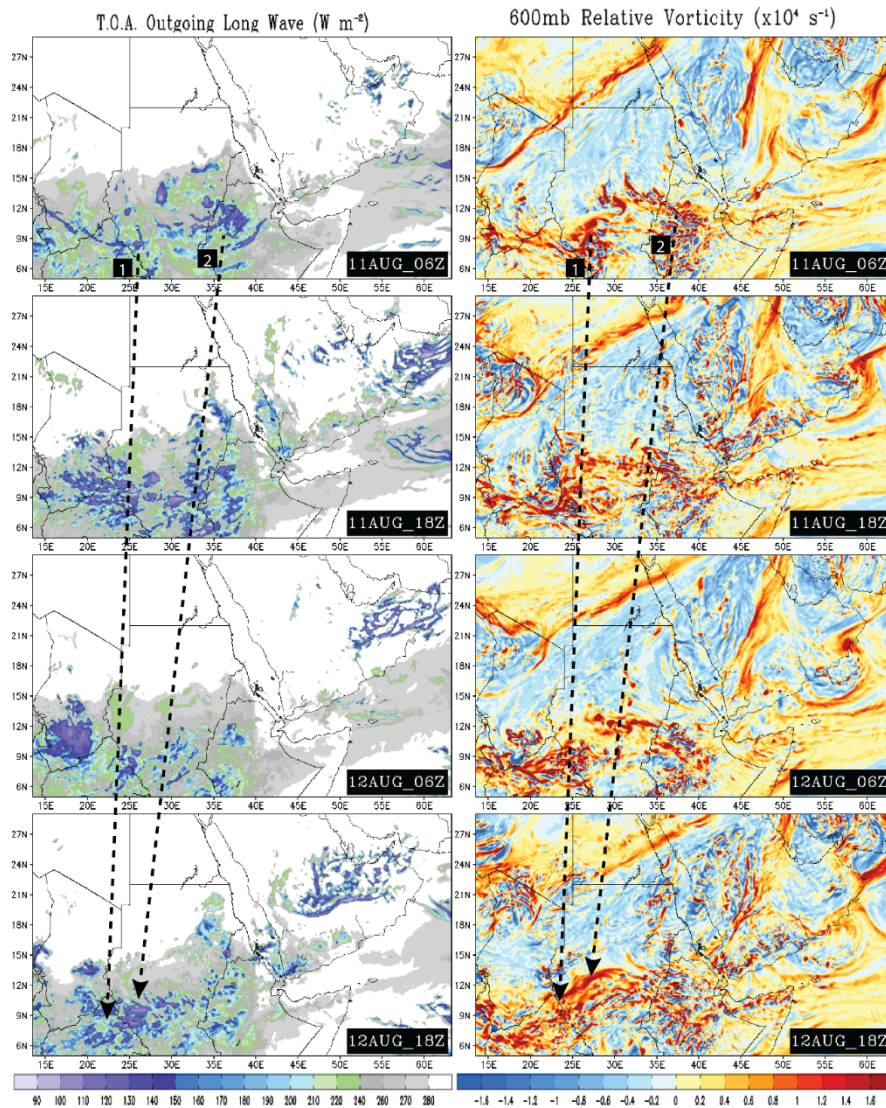


Figure 10. (b) WRF simulated top of the atmosphere outgoing long wave radiation ($W s^{-2}$) shaded in the left column and 600 mb relative vorticity ($10^{-4} s^{-1}$) shaded in the right column. Time interval is between /08/11/06Z to 08/12/18Z every 12 h.

Figure 10a illustrates the formation and evolution phase of A04's associated MCSs and vorticity from the outgoing long wave radiation (OLR) and relative vorticity field, respectively. There are two distinct areas

of orographic generated lee vorticity and convection that will contribute to the formation of A04. At 09/06Z, the convective cloud burst and vorticity perturbation at (12°N, 40°E) over the Ethiopian Highlands is denoted as MCS-1. The convective cloud burst and vorticity perturbation located at (15°N, 47°E) over the southern Arabian Peninsula is denoted as MCS-2. These MCSs will propagate to the west where they will be enhanced by the orographic effects. The biggest difference between the relative vorticity fields of the 8-km WRF simulation and the ERA-I is that the simulation resolves more orographic generated vorticities, especially during the diurnal cycles. At 09/18Z, MCS-1 and MCS-2 are being enhanced by the Ethiopian Highlands and Asir Mountains, respectively. The convective cloud burst with MCS-1 becomes better organized, while MCS-2 is propagating into East Africa by 10/06Z. At 10/18Z, the two MCSs are very noticeable by the OLR field. MCS-1 is located over South Sudan at (9°N, 30°E) and MCS-2 is located over the Ethiopian Highlands at (14°N, 37°E). During the formation stage of MCS-1 and MCS-2, the systems were propagating at the same speeds of 8.5 m s^{-1} .

During the merging phase, MCS-1 begins to propagate slower than MCS-2 (Figure 10b). At 11/06Z MCS-1 is slowing down as it nears the Darfur Mountains while MCS-2 begins to split from the Ethiopian Highlands's stationary mode of convection. Parts of MCS-1 is split by the Darfur Mountains at 11/18Z and a convective burst is seen on the lee of the Darfur Mountains at 12/06Z. Over the next 12 h, remnants of MCS-1 continue to propagate to the west at very slow speeds and MCS-2 begins to catch up. By 12/18Z MCS-1 and MCS-2 begins the merging phase, where the vorticities from both systems begin to organize with each other. During the merging phase, MCS-1 has a propagation speed of 3.4 m s^{-1} and MCS-2 has a propagation speed of 8.5 m s^{-1} .

The final stage of the formation of A04 is mature phase (Figure 10c). MCS-1 and 2 are now completely merged together and has become a coupled AEW-MCS. At 13/06Z, A04 can be seen on the lee of the Darfur Mountains as a convectively couple system with vortices. The system propagates off to the west while maintaining as an AEW-MCS until it out of the domain at 14/18Z. The propagation speed of the A04 is 8.5 m s^{-1} .

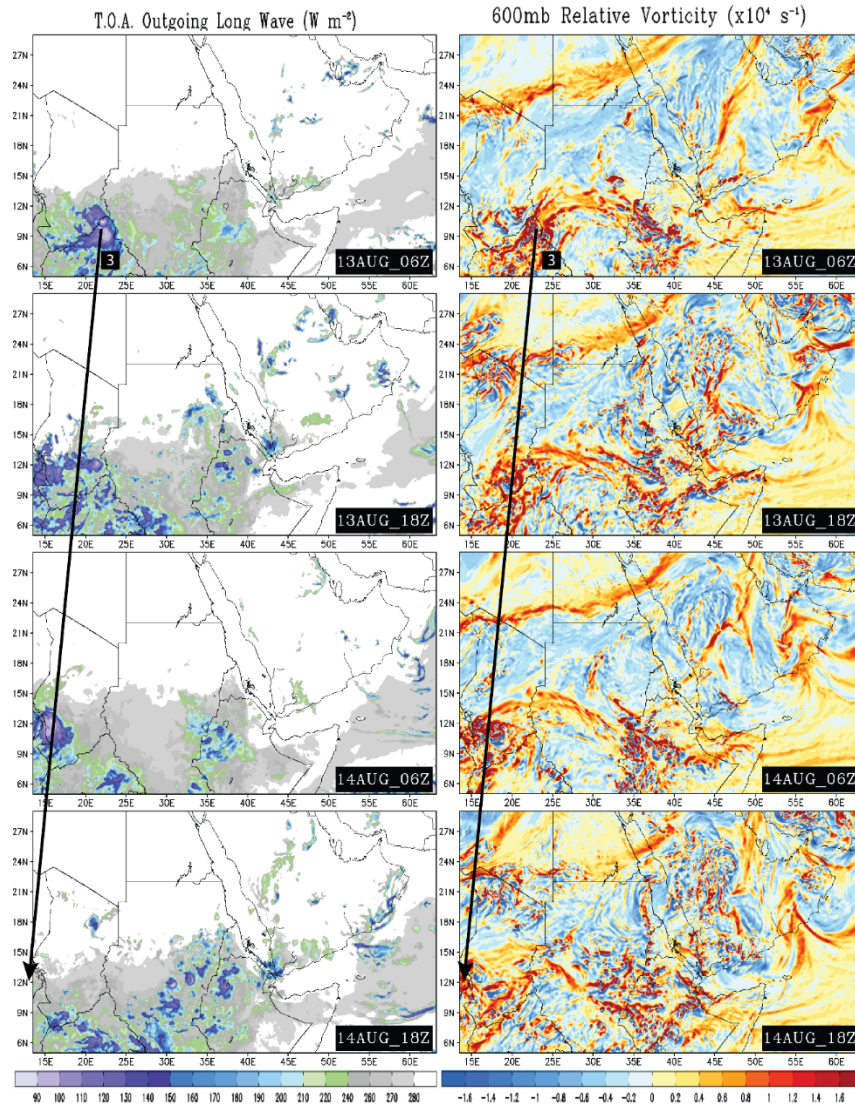


Figure 10. (c) WRF simulated top of the atmosphere outgoing long wave radiation (W s^{-2}) shaded in the left column and 600 mb relative vorticity (10^{-4} s^{-1}) shaded in the right column. Time interval is between /08/13/06Z to 08/14/18Z every 12 h.

3.2.3. Evolution of the AEJ and Embedded East Local Wind Maximum

During A04's evolution across southern Arabia and East Africa, the AEJ played a role in maintenance of the system's intensity. The AEJ have

been long understood to support the growth of AEWs through the barotropic/baroclinic mechanism (Charney and Stern 1962; Rennick 1976; Mass 1979; Thorncroft 1995, Grist et al. 2002). In recent studies, it has been found that AEWs may be triggered by MCS over the Darfur Mountains (Berry and Thorncroft 2005; Mekonnen et al. 2006), the Ethiopian Highlands (Lin et al. 2005), and the southern Arabian/Asir Mountains (Lin et al. 2013). This section attempts to show the evolution of the AEJ in East Africa and Arabian Peninsula and the growth of A04 along the jet. The triggering of A04 from MCSs and convergence was already established in the previous section 3.2.2.

The AEJ have two embed local wind maximums (LWM) located in West Africa and East Africa. The intensity of the east local wind maximum (LWM_E) at ($35^\circ E$, $15^\circ N$) has a zonal wind speed average of -9.81 m s^{-1} and the intensity of the west local wind maximum (LWM_W) at ($17^\circ W$, $18^\circ N$) has a zonal wind speed average of -13.41 m s^{-1} for the month of August (Spinks et al. 2014). In particular, the LWM_E is a contributing factor to the maintenance and propagation of easterly waves over southern Arabian and East Africa.

Figure 11 depicts the 600 mb zonal wind and geopotential heights every 24 h. The AEJ is located between $12^\circ N$ and $21^\circ N$ and is to the south of the subtropical high-pressure systems. The Arabian high can be seen centered at ($25^\circ N$, $40^\circ E$) with geopotential height values of 4460 m at 9/06Z. Easterly wind over southern Arabia is 10 to 12 m s^{-1} and a maximum located at ($15^\circ N$, $47^\circ E$), which is also associated with MCS-2's vorticity perturbation. In climatological analysis of the AEJ from previous studies, the LWM_E appears to be a stationary feature. In this case study, the LWM_E propagates along with MCS-2 from southern Arabia into East Africa while growing in intensity, reaching its maximum over Sudan. At 10/06Z, the geopotential height increases as well as the LWM_E . The AEJ will be formed at 600 mb with an elongated easterly zonal geostrophic flow generated from baroclinicity. The presence of the Arabian high will increase easterly flow to the south of the anticyclonic centers because of the increased meridional geopotential gradient.

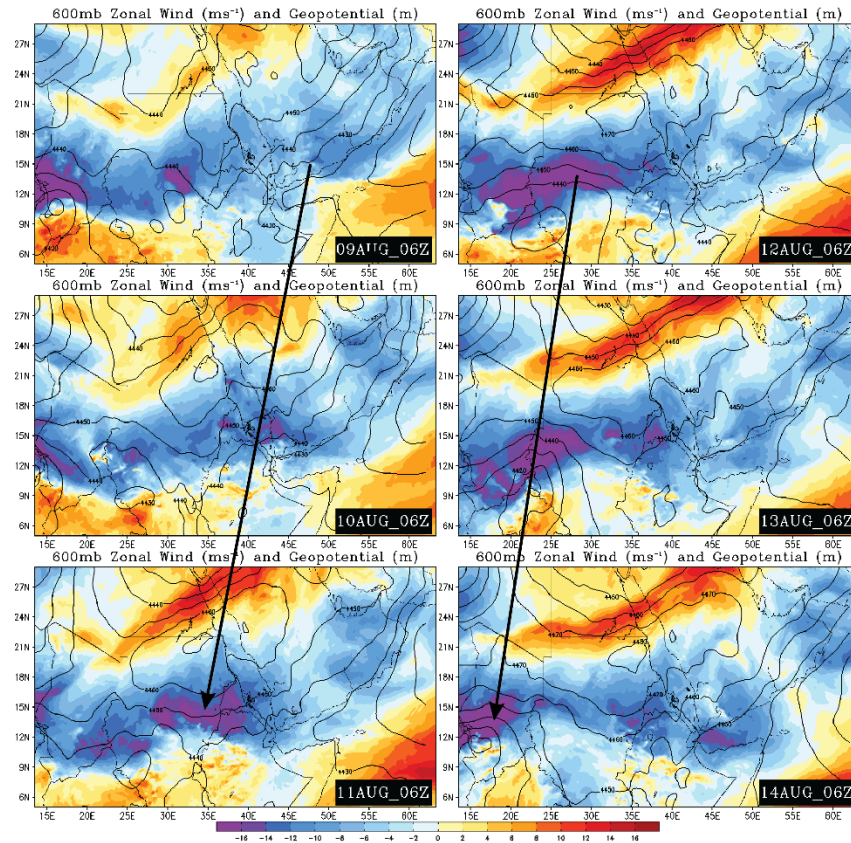


Figure 11. WRF simulated 600 mb zonal wind shaded every 2 m s^{-1} and geopotential height (m) in black contours. Time interval is between 9/06Z and 14/06Z every 24 h. The black lines denote the located of the maximum zonal winds associated with A04.

By 11/06Z, the LWM_E located at (15°N , 35°E) is in a mature phase with velocities greater than 16 m s^{-1} and the Arabian High is centered at (21°N , 35°E). This is also the start of the merging phase of MCS-1 and MCS-2 in section 3.2.2. At 12/06Z, the LWM_E located at (13°N , 27°E) and the presence of westerly wind centered at (5°N , 25°E) will increase the meridional zonal gradient and enhance easterly wave development, which can be seen at (8°N , 24°E). By 13/06Z, the LWM_E is coupled with A04 and is in a mature phase while propagating. As the systems continue to propagate to the west, the LWM_E is separated from the dominate influence

of the Arabian high and is intercepted by the Saharan high after crossing 20°E.

The LWM_E is providing maintenance to A04 from the maximum easterly wind flow induced from the Arabian high's meridional geopotential gradient. This component is essential for the survival of vorticity perturbation over the Arabian Peninsula and East Africa. The orographic generated lee vorticities are part of the stationary mode and will need the presence of easterly wind flow in order to propagate away from the mountains. Once split from the mountains, the vorticity perturbations will be able to grow under the influence of the LWM_E . The existence of the westerly wind to the south of the easterly wind will also be a contributing factor to vorticity maintenance when the zonal gradient is robust.

4. CONCLUSION

A coupled African easterly wave-mesoscale convective system was examined over the Arabian Peninsula and East Africa in August 2004. The system A04 was identified through satellite brightness temperature and ERA-I total cloud cover. A04's convective origins were found to be over the southern Arabian Peninsula and propagated in to East Africa. The vorticities field from the ERA-I was then analyzed to track A04's associated vorticity perturbation. From origin to the mature stage of A04, the propagation speed was 7.6 m s^{-1} . The formation of A04's vorticity perturbation was on 8/9/00Z located at (15°N, 47°E). A vorticity budget was then performed to investigate the formation mechanisms from the ERA-I data. It was found that the horizontal vorticity advection has the highest magnitude and convergence was the driving factor to vorticity generation. While the ERA-I provided significant findings for the formation mechanism using vorticity, it does not resolve well the orographic effects from the southern Arabian Mountains and Ethiopian Highlands.

To test the origin and formation of A04, a numerical simulation using the WRF model was employed using the ERA-I to initialize with. Higher

resolution results provided the information needed to explain the origin A04's vorticity perturbation, especially over the mountains. It was found that the higher resolution results produced a stronger zonal wind flow over East Africa and the Arabian Peninsula, which would directly increase the magnitudes of the vorticity field. There were also more vorticity processes resolved over the mountains, especially during diurnal cycles. The vorticity budget was performed on the numerical simulation and the results were as follows:

1. The overall vorticity budget from the numerical simulation increased in magnitude, with the vorticity advection having the highest order of 10^{-9} s^{-2} due to the advection along the ITCZ. A04's vorticity perturbation is highly influenced from easterly wind flow and the zonal gradient that increases vorticity intensity.
2. The convergence of planetary vorticity explains the generation of vorticity over the southern Arabian Peninsula. The Arabian high produces northerly and easterly winds over Arabia and the Indian Ocean high produces southerly and westerly winds. When these highs begin to converge, cyclonic vorticity is generated over the southern Arabian Peninsula, particularly during diurnal cycles when lee vorticities are produced from orographic effects.

A04 went through 3 phases: formation, merging, and mature. Two MCSs were associated with the formation stage, which was over the Ethiopian Highlands (MCS-1) and southern Arabian Mountains (MCS-2) at 9/06Z. These areas are part of the stationary mode of lee vorticity and convective generation from the diurnal cycle. Once generated, the MCSs propagate away from their respected mountain region. During the merging phase starting at 11/06Z, MCS-1 begins to slow down as it nears the Darfur Mountains while MCS-2 continues to propagate at a constant speed of 8.5 m s^{-1} over the Ethiopian Highlands and into Sudan. At 13/06Z, the systems have merged together over the Darfur Mountains and formed into a mature AEW-MCS. The diurnal cycle and convective cloud burst over the next 12 h enhances the systems as it continues to propagate to the west.

The east local wind maximum (LWM_E) of the Africa easterly jet was also investigated to show how A04 is maintained by easterly wind flow. As A04 propagates to the west, the easterly wind flow also increases under the influence of the Arabian high. The high-pressure system induces a strong meridional geopotential gradient that will increase easterly wind on the southern rim of the high. Once over Sudan, the LWM_E is mature and the presence of westerly wind south of the easterly wind flow will produce a stronger zonal gradient. Over Sudan is when MCS-1 and MCS-2 began to merge. Once A04 is mature and propagate to the west of the Darfur Mountains, the LWM_E will be intercepted by the influence of the Saharan high. The data analysis and numerical model simulated results are consistent with the conceptual model proposed in Lin et al. (2013).

ACKNOWLEDGMENTS

We would like to thank J. Zhang, PhD, A. Mekonnen, PhD, and L. Liu, PhD of the North Carolina A&T State University and Dr. J. Lee, PhD of the NOAA ESRL for their comments on this paper. This research was partially supported by the NOAA Educational Partnership Program under the cooperative agreement A06OAR4810187 and NSF Awards AGS-1265783, CNS-1126543, and CNS-1429464.

REFERENCES

- Berry, G. J. & Thorncroft, C. D. (2005). Case study of an intense African easterly wave. *Mon Weather Rev.*, 133, 752-766.
- Burpee, R. W. (1972). The origin and structure of easterly waves in the lower troposphere of North Africa. *J. Atmos. Sci.*, 29, 77-90.
- Burpee, R. W. (1974). Characteristics of the North African easterly waves during the summers of 1968 and 1969. *J. Atmos. Sci.*, 31, 1556-1570.
- Carlson, T. N. (1969). Synoptic histories of three African disturbances that developed into Atlantic hurricanes. *Mon. Wea. Rev.*, 97, 256-276.

- Charney, J. G. & Stern, M. E. (1962). On the stability of internal baroclinic jets in a rotating atmosphere. *J. Atmos. Sci.*, *19*, 159-172.
- Chang, C. B. (1993). Impact of desert environment on the genesis of African wave disturbances. *J. Atmos. Sci.*, *50*, 2137-2145.
- Chen, T. C. (2006). Characteristics of African easterly waves depicted by ECMWF Reanalysis for 1991-2000. *Mon. Wea. Rev.*, *134*, 3539-3566.
- Dee, D. P. et al. (2011). The ERA-Interim reanalysis: configuration and performance of the data assimilation system. *Quart. J. Roy. Meteor. Soc.*, *137*, 553-597.
- Fink, A. H. & Reiner, A. (2003). Spatio-temporal variability of the relation between African easterly waves and West African squall lines in 1998 and 1999. *J. Geophys. Res.*, *108* (D11), 4332.
- Glickman, T. S. (ed.) (2000). Glossary of Meteorology. 2nd Ed., *Amer. Meteor. Soc.*, 855pp.
- Grist, J. P., Nicholson, S. E. & Barcilon, A. L. (2002). Easterly wave over Africa. Part II: Observed and modeled contrast between wet and dry years. *Mon. Wea. Rev.*, *130*, 212-225.
- Hodges, K. I. & Thorncroft, C. D. (1997). Distribution and statistics of African mesoscale convective weather systems based on ISCCP Meteosat imagery. *Mon. Wea. Rev.*, *125*, 2821-2837.
- Hsieh, J. S. & Cook, K. H. (2005). Generation of African easterly wave disturbances, Relationship to the African easterly jet. *Mon. Wea. Rev.*, *133*, 1311-1327.
- Hsieh, J.-S. & Cook, K. H. (2007). A study of the energetics of African easterly waves using a regional climate model. *J. Atmos. Sci.*, *64*, 2212-2230.
- Knapp, K. R., Ansari, S., Bain, C. L., Bourassa, M. A., Dickinson, M. J., Funk, C., Helms, C. N., Hennon, C. C., Holmes, C. D., Huffman, G. J., Kossin, J. P., Lee, H.-T., Loew, A. & Magnusdottir, G. (2011). Globally gridded satellite (GridSat) observations for climate studies. *Bull. Amer. Meteor. Soc.*, *92*, 893-907.
- Kwon, H. J. (1989). A re-examination of the genesis of African waves. *J. Atmos. Sci.*, *46*, 3621-3631.

- Laing, A. G. & Fritsch, J. M. (1993). Mesoscale convective complexes in Africa. *Mon. Wea. Rev.*, *121*, 2254-2263.
- Laing, A. G., Trier, S. B. & David, C. A. (2012). Numerical simulation of episodes of organized convection in tropical northern Africa. *Mon. Wea. Rev.*, *140*, 2874-2886.
- Landsea, C. W. (1993). A climatology of intense (or major) Atlantic hurricanes. *Mon. Wea. Rev.*, *121*, 1703-1713.
- Lin, Y. L., Robertson, K. E. & Hill, C. M. (2005). Origin and propagation of a disturbance associated with an African easterly wave as a precursor of Hurricane Alberto (2000). *Mon. Wea. Rev.*, *133*, 3276-3298.
- Lin, Y. L. (2007). *Mesoscale Dynamics*. Cambridge University Press, 630 pp.
- Lin, Y.-L., Liu, L., Tang, G., Spinks, J. & Jones, W. (2013). Origin of the pre-Tropical Storm Debby (2006) African easterly wave-mesoscale convective system. *Meteor. Atmos. Phys.*, *120* (1-2), 123-144.
- Mass, C. (1979). A linear primitive equation model of African wave disturbances. *J. Atmos. Sci.*, *36*, 2075-2092.
- Mekonnen, A., Thorncroft, C. D. & Aiyyer, A. R. (2006). Analysis of convection and its association with African easterly waves. *J. Climate*, *19*, 5405-5421.
- Mozer, J. B. & Zehnder, J. A. (1995). Lee vorticity production by large-scale tropical mountain ranges. part ii: a mechanism for the production of African waves. *J. Atmos. Sci.*, *53*, 539-549.
- Payne, S. W. & McGarry, M. M. (1977). The relationship of satellite inferred convective activity to easterly waves over West Africa and the adjacent ocean during phase III of GATE. *Mon. Wea. Rev.*, *10*, 413-420.
- Pielke, Jr., R. A. & Landsea, C. W. (1998). Normalized hurricane damages in the United States: 1925-95. *Weather Forecasting*, *13*, 621-631.
- Rao, P. G., Hatwar, H. R., Al-Sulaiti, H. H. & Al-Mulia, A. H. (2003). Summer Shamals over the Arabian Gulf. *Weather*, *58*, 472-478.

- Reed, R. J., Norquist, D. C. & Recker, E. E. (1977). The structure and properties of African wave disturbances as observed during Phase III of GATE. *Mon. Wea. Rev.*, *105*, 317-333.
- Rennick, M. A. (1976). The generation of African waves. *J. Atmos. Sci.*, *33*, 1955-1969.
- Simmons, A. J. (1977). A note on the instability of the African easterly jet. *J. Atmos. Sci.*, *34*, 1670-1674.
- Skamarock, W. C., Klemp, J. B., Dudhia, J. D., Gill, O., Barker, D. M., Duda, M. G., Huang, X.-Y., Wang, W. & Powers, J. G. (2008). A description of the advanced research WRF version 3. NCAR technical note, 113 pp.
- Thorncroft, C. D. & Hoskins, B. J. (1994a). An idealized study of African easterly waves. Part I: a linear view. *Quart. J. Roy. Meteor. Soc.*, *120*, 953-982.
- Thorncroft, C. D. & Hoskins, B. J. (1994b). An idealized study of African easterly waves. Part II: a nonlinear view. *Quart. J. Roy. Meteor. Soc.*, *120*, 983-1015.
- Thorncroft, C. D. (1995). An idealized study of African easterly waves. Part III: more realistic basic states. *Quart. J. Roy. Meteor. Soc.*, *121*, 1589-1614.
- Thorncroft, C. D., Hall, N. M. & Kiladis, G. N. (2008). Three-dimensional structure and dynamics of African easterly waves. Part III: genesis. *J. Atmos. Sci.*, *65*, 3596-3607.